

# UC Davis

## UC Davis Previously Published Works

### Title

Symmetry-enforced Fermi surface degeneracies observed in the purported time-reversal symmetry-broken superconductor LaNiGa<sub>2</sub>

### Permalink

<https://escholarship.org/uc/item/9qz8p51b>

### Journal

Physical Review B, 110(16)

### ISSN

2469-9950

### Authors

Staab, Matthew

Prater, Robert

Sreedhar, Sudheer

et al.

### Publication Date

2024-10-01

### DOI











10.1103/physrevb.110.165115

### Copyright Information

This work is made available under the terms of a Creative Commons Attribution License, available at <https://creativecommons.org/licenses/by/4.0/>

Peer reviewed

## Symmetry-enforced Fermi surface degeneracies observed in the purported time-reversal symmetry-broken superconductor $\text{LaNiGa}_2$

Matthew Staab <sup>1</sup>, Robert Prater <sup>1</sup>, Sudheer Sreedhar <sup>1</sup>, Journey Byland <sup>1</sup>, Eliana Mann <sup>1,2</sup>, Davis Zackaria,<sup>1</sup> Yunshu Shi,<sup>1</sup> Henry J. Bowman,<sup>1</sup> Andrew L. Stephens <sup>1</sup>, Myung-Chul Jung <sup>3</sup>, Antia S. Botana <sup>3</sup>, Warren E. Pickett,<sup>1</sup> Valentin Taufour <sup>1</sup>, and Inna Vishik <sup>1,\*</sup>

<sup>1</sup>*Department of Physics and Astronomy, University of California, Davis, Davis, California 95616, USA*

<sup>2</sup>*John A. Paulson School of Engineering and Applied Sciences, Harvard University, Cambridge, Massachusetts 02138, USA*

<sup>3</sup>*Department of Physics, Arizona State University, Tempe, Arizona 85281, USA*



(Received 18 December 2023; revised 2 August 2024; accepted 5 September 2024; published 7 October 2024)

$\text{LaNiGa}_2$  is a superconductor that has been shown to break time-reversal symmetry in the superconducting state without any known nearby magnetism. Recently, single crystals of  $\text{LaNiGa}_2$  have been synthesized, revealing a nonsymmorphic  $Cmcm$  space group. Here, we report on measurements of the electronic structure of  $\text{LaNiGa}_2$  throughout the three-dimensional Brillouin zone (BZ) using angle-resolved photoemission spectroscopy. Our findings show broad consistency with density functional theory calculations and provide evidence for degeneracies in the electronic structure that are predicted from the space group symmetry. We report evidence for those predicted symmetry-enforced degeneracies as well as accidental near degeneracies throughout the BZ. These degeneracies and near degeneracies may play a role in the pairing mechanism of  $\text{LaNiGa}_2$ . Our results provide insight into the interplay between structure, fermiology, and superconductivity in unconventional superconductors with nonsymmorphic space group.

DOI: [10.1103/PhysRevB.110.165115](https://doi.org/10.1103/PhysRevB.110.165115)

### I. INTRODUCTION

Unconventional superconductors have mechanisms or phenomena that differ from superconductors described by Bardeen-Cooper-Schrieffer (BCS) theory. The normal-state electronic properties of unconventional superconductors can inform their superconducting mechanism as well as identify factors that raise or lower the transition temperature  $T_c$ . For example, the experimentally established fermiology of iron-based superconductors influenced early proposals of interband pairing [1,2], and in cuprate high-temperature superconductors, the normal-state pseudogap presents one of the most formidable challenges to establishing the superconducting mechanism [3,4]. Among superconductors that have been reported to break time-reversal symmetry below  $T_c$ ,  $\text{Sr}_2\text{RuO}_4$  has been the most heavily investigated, and its normal-state band structure, particularly the van Hove singularity [5,6], has been implicated in the origin of superconductivity and the evolution of  $T_c$  under strain [7]. In other classes of superconductors, there are examples of isostructural materials that alternately break/maintain time-reversal symmetry in the superconducting state, providing further indication that details of fermiology can play a role in the pairing state [8].

Time-reversal symmetry-breaking (TRSB) superconductivity is relatively rare, with only several dozen single-material (not heterostructure) candidates identified to date [9,10], and many of these compounds have magnetism or magnetic fluctuations which may play a role in mediating TRSB superconductivity [11–13].  $\text{LaNiGa}_2$  is a rare example where

magnetism is absent due to the Ni bands being filled [14,15]. This material has a superconducting transition temperature  $T_c \approx 2$  K [16], and most prior studies have been performed on polycrystalline specimens.  $\mu\text{SR}$  experiments reported the onset of spontaneous magnetization below  $T_c$ , interpreted as demonstrating TRSB superconductivity [17].

The recent synthesis of single crystals has enabled a wider array of experiments to understand structural, thermodynamic, and electronic properties relevant to the superconducting mechanism [10]. More than enabling new experiments, these single crystals demonstrated that the space group was previously misidentified as  $Cmmm$ , with the correct space group being  $Cmcm$ , which is nonsymmorphic. The  $Cmcm$  space group imposes symmetry-enforced degeneracies at the  $k_z$  Brillouin zone (BZ) boundary [Z-T-A plane, Figs. 1(a) and 1(b)]. Spin-orbit coupling (SOC) splits this degeneracy everywhere except for the  $k_x = 0$  line on that plane but only slightly [14]. The symmetry-enforced degeneracies and near degeneracies of this space group are predicted to have involvement in the order parameter in  $\text{LaNiGa}_2$  [14], and nonsymmorphic symmetries may more generally enhance  $T_c$  for odd parity superconducting states [18].

Other materials in the  $Cmcm$  space group have recently garnered attention due to the degenerate features of their band structures.  $\text{TaNiTe}_5$  and  $\text{TaPtTe}_5$  are two such examples of nonsuperconducting  $Cmcm$  crystals that have been shown by angle-resolved photoemission spectroscopy (ARPES) to have Dirac nodal lines at the BZ boundary [19,20]. Being nonsuperconducting, these compounds show that it is not just the space group and related Fermi surface (FS) degeneracies that make  $\text{LaNiGa}_2$  a superconductor.

Here, we present the experimental normal-state electronic structure of purported TRSB superconductor  $\text{LaNiGa}_2$

\*Contact author: [ivishik@ucdavis.edu](mailto:ivishik@ucdavis.edu)

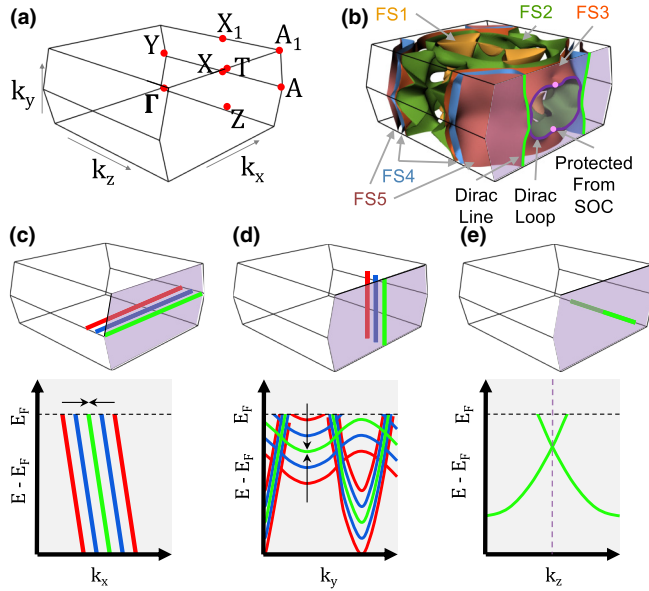


FIG. 1. Predicted fermiology and nodal plane features. (a) The base centered orthorhombic Brillouin zone (BZ) with high-symmetry points and axes labeled. The purported nodal plane is the  $k_z$  boundary or the  $Z$ - $T$ - $A$  plane, colored in purple in (b)–(e). (b) The five Fermi surfaces of  $\text{LaNiGa}_2$  shown in the BZ, reproduced from Ref. [10]. The pink dots indicate the spin-orbit coupling (SOC)-protected nodal points. Features labeled “nodal line” and “nodal loop” are degenerate crossings at  $E_F$  that get split by SOC. (c)–(e) Schematic of predicted band structure when accessing the nodal plane three different ways. (c) and (d) cuts parallel to the nodal plane are expected to show band merging in energy and momentum. (e) When piercing the predicted nodal plane, parallel to  $k_z$ , the calculations predict a Dirac crossing of bands.

throughout the entire three-dimensional (3D) BZ, as measured by ARPES. The following results are presented: (1) broad agreement between density functional theory (DFT) and measured electronic structure throughout the 3D BZ; (2) evidence for FS degeneracies on the  $Z$ - $T$ - $A$  plane, within resolution of experiment, via distinct bands merging into one approaching this plane in parallel [Figs. 1(c) and 1(d)]; (3) evidence of predicted linear crossings of all bands when cutting perpendicular to the  $Z$ - $T$ - $A$  plane [Fig. 1(e)]; and (4) evidence for near degeneracies of bands throughout the BZ separate from those on the  $Z$ - $T$ - $A$  plane. The relevance of these features to the proposed mechanism of unconventional superconductivity are discussed.

## II. METHODS

### A. Crystal growth and ARPES measurements

The samples were grown using the technique described in the original single-crystal growth by Badger *et al.* [10]. ARPES measurements were performed at Stanford Synchrotron Radiation Lightsource (SSRL) beamline 5-2. Samples were cleaved *in situ* at pressure better than  $5 \times 10^{-11}$  Torr and at temperatures  $< 15$  K. The photon energy was varied as stated in relevant figures. The energy and momentum resolution of the experiments were 25 meV and  $\approx 0.01 \text{ \AA}^{-1}$ ,

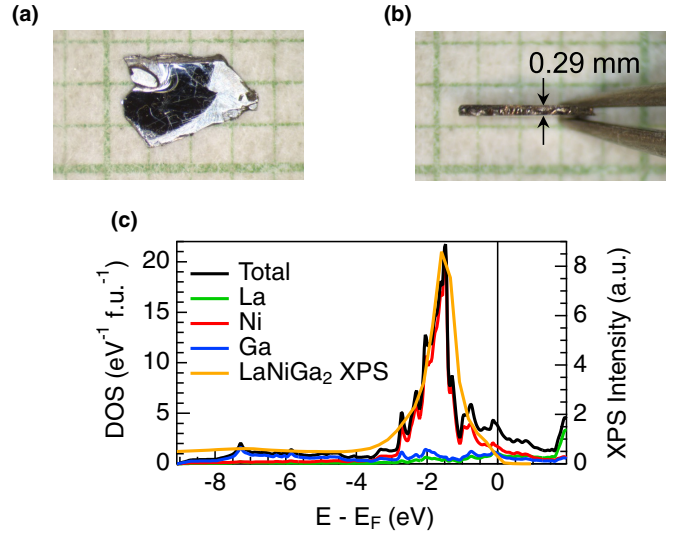


FIG. 2. Sample dimensions and x-ray photoelectron spectroscopy (XPS). (a)  $\text{LaNiGa}_2$  sample pictured on millimeter paper showing typical shape and size of the platelet crystals in the  $a$ - $c$  plane (natural orientation). (b) Image of the sample held on its side (thin-edge orientation). (c) Projected density of states calculations along with XPS measured with 144 eV photons in the natural orientation.

respectively. The beam spot size was  $\sim 20 \times 30 \mu\text{m}$  (microARPES) for all experiments.

$\text{LaNiGa}_2$  single crystals grow in a platelet shape with typical dimensions of  $2 \times 2 \times \lesssim 0.3 \text{ mm}$  [Figs. 2(a) and 2(b)]. The platelet-shaped samples are most naturally cleaved by mounting a ceramic top post on top of the platelet, hereafter called the *natural-cleave* orientation. Cleaving the crystal in the natural orientation allows for ARPES that approximately probes of planes of constant  $k_y$ . To probe band structure at roughly constant values of  $k_z$  or  $k_x$  without relying exclusively on the lower-resolution photon energy tuning method, we mounted the platelet samples on their thin edge. This was done by etching a groove into the sample holder and adhering the sample into the groove. The samples were mounted into the groove with ultrahigh vacuum compatible Loctite and a conductive pathway created with the silver epoxy Epo-tek H21D.

For data shown here, the samples were prealigned using Laue (see the Supplemental Material [21]) to have the  $\vec{a}$  axis normal to the sample holder. The thin-edge-mounted samples were broken *in situ* using a flat-edged wobble stick to apply uniform pressure across the face without using a top post. This configuration of thin-edge cleaving was used to probe the  $k_y$  dependence of the electronic structure directly with ARPES. Due to the small size of the cleaved regions that arise from the thin-edge method, microARPES is crucial for enabling measurements of these samples.

### B. Electronic structure calculations

DFT calculations were carried out using the full-potential linearized augmented plane-wave code WIEN2K [22]. We used the Perdew-Burke-Ernzerhof (PBE) version of the generalized gradient approximation as the exchange-correlation functional [23]. The atomic coordinates used for these calculations were

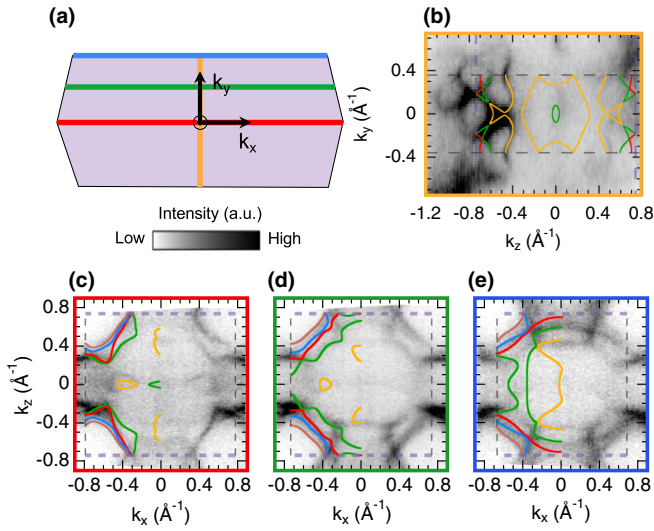


FIG. 3. Observed fermiology for selected planes in the Brillouin zone (BZ). (a) Projection of the BZ showing locations of the planes with colored lines corresponding to the borders in (b)–(e). (b) Constant energy map integrated 45 meV around the Fermi energy at 144 eV in the thin-edge orientation. (c)–(e) Angle-resolved photoemission spectroscopy (ARPES) constant energy maps integrated 50 meV around the Fermi energy. Measured in the natural platelet orientation at 116, 124, and 132 eV, respectively, to access the center, predicted  $k_y$  of the spin-orbit coupling (SOC)-protected nodal point, and the top of the BZ. Density functional theory (DFT)-calculated Fermi crossings shown in (b)–(e) are colored corresponding to the Fermi surfaces in Fig. 1. In (c)–(e), they are only overlaid on half of the zone for clarity of the data. Purple plane in (a) and dashed lines in (b)–(e) indicate  $Z$ - $T$ - $A$  plane location. Black dashed lines indicate the other boundary of the BZ.

those listed in Refs. [10,14]. The muffin-tin sphere sizes were 2.50 a.u. for La, 2.32 a.u. for Ni, and 2.20 a.u. for Ga. The plane-wave cutoff was determined by  $R_{mt}^{\min} K_{\max} = 7$ , and the  $k$ -point mesh used was  $34 \times 34 \times 33$ . The effects of SOC were included by using the second variational method as implemented in WIEN2K.

### III. RESULTS

Figure 2(c) shows an angle-integrated valence band spectrum, together with calculated partial and total density of states (DOS). These x-ray photoelectron spectroscopy (XPS) data are collected on the same natural cleave as ARPES data. Maps of constant energy at the Fermi level ( $E_F$ ), yielding FS maps, are shown for four characteristic planes in momentum space in Fig. 3. The associated DFT calculations are partially superimposed to establish the alignment between theoretical and experimental fermiology. The displayed planes of the BZ are schematically shown in Fig. 2(a) by orange, red, green, and blue lines which correspond to (b)  $k_x = 0$  (144 eV), (c)  $k_y = 0$  (116 eV), (d)  $k_y = 0.516 \cdot 2\pi/b$  (124 eV), and (e)  $k_y = 2\pi/b$  (132 eV), respectively (see Ref. [10] for structural parameters). Data for Fig. 2(b) were collected in the thin-edge orientation directly probing the  $k_x = 0$  plane, which permits spectra orthogonal to the purported nodal plane. Broader photon energy dependence was performed from 110 to 144 eV and is shown in the Supplemental Material [21], where meth-

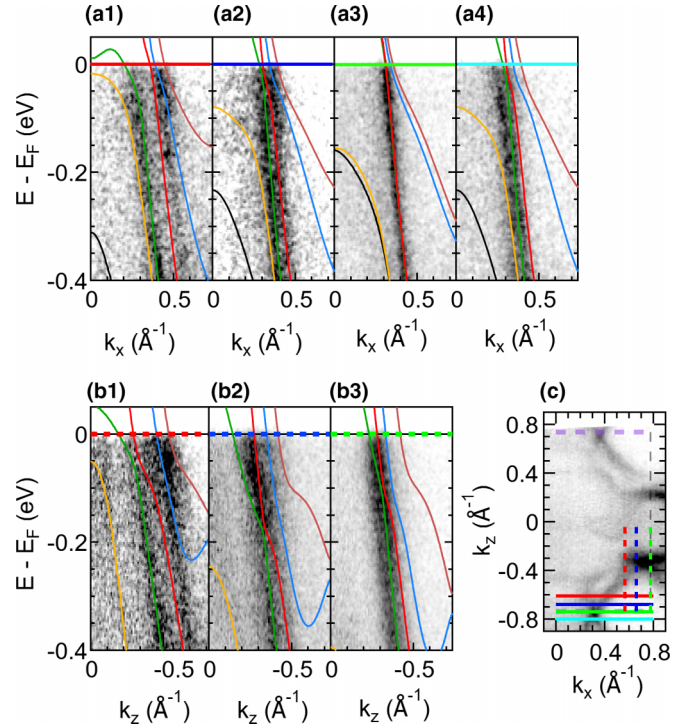


FIG. 4. Band merging in momentum at zone boundaries. (a1)–(a4) Spectra approaching (a1), (a2) at (a3), and beyond (a4), the  $Z$ - $T$ - $A$  plane as a function of  $k_z$ . (b1)–(b3) Spectra approaching (b1), (b2), and on (b3), the Brillouin zone (BZ) boundary along  $k_x$ . (c) Constant energy map at the Fermi level indicating the location of the spectra in (a) and (b). (a) and (b) Density functional theory (DFT)-predicted bands are overlaid according to the color of the Fermi surface (FS) they create in Fig. 1. All spectra collected with 120 eV photons.

ods for establishing the relationship between photon energy and  $k_{\perp}$  (momentum perpendicular to surface plane) are also addressed (see also Ref. [24] for more discussion).

One defining feature of the predicted electronic structure is pairs of bands merging together when approaching the  $Z$ - $T$ - $A$  plane with parallel cuts. This is shown in Fig. 4 and contrasted with spectra near the orthogonal zone boundary. Figures 4(a1)–4(a4) show the spectra approaching (a1), (a2), on (a3), and past (a4), the predicted nodal plane. Figure 4(b) similarly shows the spectra approaching (b1), (b2), and on (b3), the zone boundary orthogonal to the predicted nodal plane. Figure 4(c) shows the described locations of the cuts in Figs. 4(a) and 4(b) overlaid with a constant energy map integrated  $\pm 50$  meV around the Fermi level. Figure 4(a) has two separated bands in panels (a1), (a2) that appear to merge in panel (a3) and split again in (a4). Figure 4(b) also shows two well-separated bands in panel (b1) that closely approach each other in panel (b3). Whereas spectra in Figs. 4(a2) and 4(b2) have similar linewidth, the spectrum in Fig. 4(a3) is considerably sharper than in Fig. 4(b3). Calculated electronic structure for these cuts is overlaid with their color corresponding to the FS number given in Fig. 1.

With the thin-edge cleave perpendicular to  $k_x$ , we can visualize bands merging in energy approaching the  $Z$ - $T$ - $A$  plane because the observed bands have band bottoms at lower binding energy. In Fig. 4, we only discuss merging

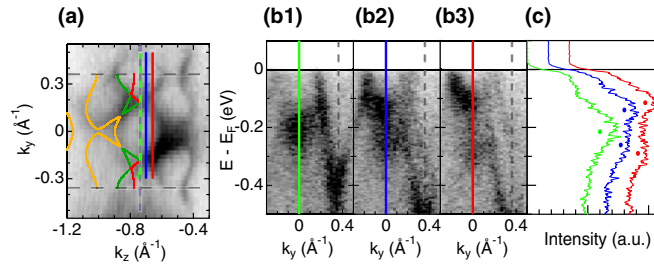


FIG. 5. Band merging in energy, thin-edge cleave. (a) Fermi level constant energy contour cropped from Fig. 3(b) showing locations of cuts in (b1)–(b3). Black and purple dashed lines indicate Brillouin zone (BZ) boundaries. (b1)–(b3) Angle-resolved photoemission spectroscopy (ARPES) spectra at three parallel cuts. (c)  $k_y = 0$  energy distribution curves (EDCs) of (b1)–(b3) in green, blue, and offset for clarity. Dots in (c) are guides to the eye for peak position.

in momentum because the band bottoms are well below the displayed energy range. Nevertheless, for cuts approaching the purported nodal plane in parallel, bands always merge in both energy and momentum. Figure 5 shows spectra along three parallel cuts moving progressively further from the zone boundary [panels (b1)–(b3)]. In Fig. 5(c), we compare energy distribution curves (EDCs) at the  $k_y = 0$  point, where a band bottom is located. Figure 5(b1), taken along the zone boundary, shows a single band in the spectrum and a single peak in the EDC. As one moves away from the zone boundary, the bands split in two, as seen both in the image plots and the EDCs. The magnitude of this split is  $\approx 200$  meV for cuts differing by  $\approx 6\%$  of the BZ.

So far, we have provided evidence for band degeneracy at the  $Z$ - $T$ - $A$  plane by investigating the spectra along lines parallel to the  $Z$ - $T$ - $A$  plane. The second predicted signature of the  $k_z$  BZ boundary is that, for all cuts perpendicular to it, all bands which cross the  $Z$ - $T$ - $A$  plane should do so with a Dirac-like (linear) crossing, up to SOC. In Fig. 6(a), we show a spectrum along the  $k_z$  axis that shows a Dirac-like crossing at the  $Z$ - $T$ - $A$  (purple dashed line) 0.2 eV below  $E_F$ . That spectrum, being along the  $k_z$  axis, intercepts the nodal plane along the  $Z$ - $T$  line and is therefore predicted to be protected against SOC splitting due to an additional symmetry. In Figs. 6(b1)–6(b3), we show three parallel cuts that intersect the  $Z$ - $T$ - $A$  plane successively closer to the purported nodal line. In the experimental spectra, two linear crossings are clearly seen in Fig. 6(b1), which successively move to lower binding energy approaching the momentum marked by the X-shaped feature in the FS map in Fig. 6(c). Finally, at the purported nodal line in Fig. 6(b3), a linear crossing is observed right at  $E_F$ . The crossings in Fig. 6(b) are not protected from SOC and are therefore gapped, but their gap size too small to be resolved with the present experiments. The bottom of Figs. 6(a) and 6(b) show the DFT-calculated dispersion in the corresponding locations.

#### IV. DISCUSSION

We begin by addressing the lack of magnetism in  $\text{LaNiGa}_2$ , previously justified by filled Ni  $3d$  bands. In the DOS from DFT calculations, these filled bands yield a large peak at  $\approx 1.8$  eV binding energy in Fig. 2(c). The measured XPS

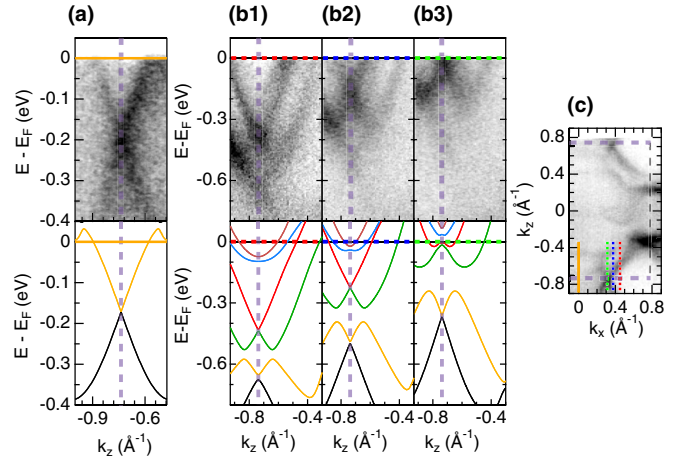


FIG. 6. Linear crossings for cuts perpendicular to nodal plane. (a) Thin-edge orientation spectrum taken along the  $\Gamma$ - $Z$  line at a photon energy of 144 eV. (b) Spectra taken in the natural orientation with 120 eV photons near a Fermi crossing at the zone boundary. (c) Constant energy contour from the natural orientation indicating the location of cuts in (a) and (b). The cut from (a) is at  $k_y = 0 \text{ \AA}^{-1}$  while those from (b) and (c) are at  $k_y \approx 0.09 \text{ \AA}^{-1}$ . (a) and (b) (bottom) Density functional theory (DFT)-predicted bands are shown according to the color of the Fermi surface (FS) they create in Fig. 1.

intensity, a rough proxy for the DOS, is consistent with this calculated feature, supporting the stated absence of magnetism in this compound. We also note that recent nuclear magnetic/quadrupolar resonance and magnetization measurements in the normal state further do not find evidence of magnetic fluctuations or enhanced paramagnetism [25].

We now turn to the measured band structure, where we observe overall good agreement between DFT and experiment throughout the 3D BZ. We note strong matrix element effects [26], which is the reason why certain bands are observed more, less, or not at all in certain regions of the BZ. An example of this is FSs 4 and 5 in Fig. 4, where the photoemission signal from the bands that form FSs 4 and 5 (blue and maroon) are not seen in the displayed cuts. In that region of the BZ, FSs 2 and 3 have primarily  $d$ -orbital character, while FSs 1, 4, and 5 are primarily of  $p$ -orbital character (see the Supplemental Material [21]), and this difference in orbital character is the likely reason that we do not observe FSs 4 and 5.

For bands that are visible in the data, there are minor discrepancies between measured and predicted bands, particularly in the most 3D bands which form FSs 1 and 2. This can be seen in Fig. 3(c), where the teardrop-shaped pocket of FS 1 near  $k_x = -0.4 \text{ \AA}^{-1}$  is observed to be larger than predicted. Further, in Fig. 3(d), we observe elongated features of FSs 1 and 2 that appear like those of Fig. 3(e). The more two-dimensional (2D) FSs (FSs 3–5), when visible, show no substantial disagreement with the predicted electronic structure. Additionally, FSs 1 and 2 show strong agreement with predictions in the thin-edge cleave shown in Fig. 3(b).

The disagreements seen of FSs 1 and 2 are then either (1) real features of the electronic structure not captured by the calculations and constrained to only small portions of the BZ or (2) artifacts arising from the photoemission process due to momentum uncertainty in the  $k_{\perp}$  direction.

Arguing against scenario (1), there is very good agreement between ARPES FSs and DFT with regards to FSs 1 and 2 in the thin-edge cleave data. Elaborating on (2), the short inelastic mean free path (IMFP) of electrons makes ARPES a surface-sensitive measurement in the present range of photon energies. We calculate the IMFP of electrons with kinetic energy of 110 eV traveling through  $\text{LaNiGa}_2$  to be  $\lambda = 5 \text{ \AA}$  using a common empirical method [27]. This IMFP leads to an appreciable quantum uncertainty of the perpendicular momentum  $\Delta k_{\perp} = 1/\lambda = 0.2 \text{ \AA}^{-1}$  [28], comprising  $\approx 25\%$  of the BZ along  $k_y$ . Additionally, in ARPES measurements, there can be preferential sampling of bands which are being probed by the spectrometer slit normal to their constant-energy surface. These two effects— $k_{\perp}$  broadening and extremum-selective sampling—may explain the discrepancies observed in Fig. 3 as the extremum position observed for FS 1 is at  $k_y \approx 0.016 \text{ \AA}^{-1}$ .

Now we turn to focus on the observed features at the purported nodal plane. The first observation is bands merging when approaching the  $Z$ - $T$ - $A$  plane with parallel cuts (Figs. 4 and 5). While the calculations predict SOC splitting of the bands along the nodal plane at all positions except the  $Z$ - $T$  line, the splitting is extremely small in most locations. In Fig. 4(a3), the splitting between FSs 2 and 3 is 5 meV, much smaller than our experimental resolution. Also predicted are Dirac-like crossings for all bands when piercing the nodal plane in perpendicular. This is observed for several distinct bands in Fig. 6. Momentum-space band merging can be additionally visualized in FS maps, particularly in Figs. 3(c)–3(e), 4(c), and many other examples shown in the Supplemental Material [21]. These show an X-shaped feature at the BZ boundary along one direction ( $k_z$ ) but not along the other ( $k_y$ ), consistent with the location of the nodal plane. Notably, most of these observations are discernible from data alone, independent from comparison with DFT calculations.

Beyond the nodal plane, we also present evidence for near degeneracies throughout the BZ. These near degeneracies are particularly persistent at the orthogonal zone boundary ( $k_x$ ). FSs 2 and 3 have near degeneracies not only along the orthogonal BZ boundary but within the BZ at many values of  $k_y$ . Near degeneracies are observed in both the thin-edge FS as well as broad ranges of the photon energy-dependent natural-cleave fermiology. Four clear examples can be seen of near degeneracies within the BZ in Fig. 3: First, panel (b) shows degeneracy of FSs 2 and 3 at  $k_z \approx -0.65 \text{ \AA}^{-1}$ . Second, panel (c) shows a near degeneracy of FSs 2 and 3 at  $k_x \approx -0.55 \text{ \AA}^{-1}$ , where the bands are nearly coincident until they reach the  $k_x$  zone boundary. Third, panel (d) shows FSs 2 and 3 again nearly degenerate near the  $k_x$  boundary. Finally, panel (e) again shows FSs 2 and 3 being nearly degenerate inside the BZ at  $k_z \approx -0.35 \text{ \AA}^{-1}$  nearly collocated with a near degeneracy of FSs 3 and 4.

We now connect these results to prior work on this material. Early experiments have laid out a set of constraints for the pairing symmetry and mechanism of  $\text{LaNiGa}_2$ . The point group symmetry of the crystal structure, which remains unchanged with the newly assigned space group, only permits four order parameters that break time-reversal symmetry [14,17]. All are nonunitary, and all have weak SOC, the latter constraint which is confirmed with the present data. Addition-

ally, heat capacity and superfluid density were shown to be inconsistent with nodes of any kind and demonstrated to be more consistent with a two-gap model than a single-gap BCS fitting [10,29,30].

Together, these results point to a fully gapped triplet state. The Cooper pair wave function must be odd overall to comport with fermion exchange, so an even spin component implies an odd spatial component. This presents a problem when one includes information about the fermiology, as an odd spatial wave function must change sign across the  $\Gamma$  point, so a FS that encloses  $\Gamma$  should have a node, inconsistent with experiments. The calculated fermiology based on both the previous  $Cmmm$  [15] and refined  $Cmcm$  [10,14] crystal structure includes FSs which envelop the  $\Gamma$  point. In the present calculation, this includes a small pocket of FS 1 as well as FSs 2 and 3. Previously, this apparent inconsistency was resolved by considering the multiband nature of this material, wherein triplet pairing between nearly degenerate FSs can ensure an overall odd wave function [31], if the order parameter changes sign upon swapping band index. This proposed internally anti-symmetric nonunitary triplet pairing (INT) state is consistent with  $\mu$ SR indications of triplet pairing [17], nodeless superconducting gap [10,29], two superconducting gaps [30], and insensitivity of superconductivity to non-magnetic impurities [32]. We acknowledge that besides the  $\mu$ SR work, the other experimental results could also be consistent with a conventional superconducting pairing.

In this paper, we add experimentally motivated plausibility to that argument and propose further experiments to understand and optimize superconductivity in  $\text{LaNiGa}_2$ . The  $Cmcm$  space group imposes symmetry-enforced degeneracies along one plane of the BZ, the so-called *nodal plane*. Our experiments find support for this in three ways: bands merging in momentum approaching the nodal plane with parallel cuts (Fig. 4), bands merging in energy approaching the nodal plane with parallel cuts (Fig. 5), and all cuts perpendicular to the nodal plane yielding Dirac-like crossings for all bands at all energies (Fig. 6). Although SOC lifts this degeneracy on most of the nodal plane, there are still three sources of degeneracy and near degeneracy to support interband pairing: (1) symmetry-enforced exact degeneracy at predicted nodal points along the  $Z$ - $T$  line, (2) near degeneracy on nodal lines and nodal loop arising from symmetry coupled with a small (meV) amount of SOC, and (3) accidental near degeneracies included on the  $k_x$  BZ boundary [Fig. 4(b)]. The latter was present in band structure calculations based on the previous  $Cmmm$  structure, but the former two are a consequence of the  $Cmcm$  structure. The overall strong agreement between DFT calculations and experiment throughout the 3D BZ further supports the prediction of a nodal plane as well as the presence of only weak SOC [17], which is required for the experimentally compatible pairing states.

Despite the growing body of knowledge on  $\text{LaNiGa}_2$ , accelerated by the availability of single crystals, questions remain. Interband pairing benefits from near degeneracies throughout the BZ; the ones on the nodal plane will remain if the space group remains unchanged, but the ones outside the nodal plane may be tunable by uniaxial strain. The effect of this tuning on  $T_c$  can further confirm the pairing mechanism that appears to be supported by a plurality of experiments.

Moreover, it can clarify if there are pairing interactions outside of electron-phonon [33] which is the primary candidate in LaNiGa<sub>2</sub>, such as originating magnetic phases which often accompany TRSB superconductor. As an example of this, LaNiC<sub>2</sub> was also thought to be entirely nonmagnetic, until pressure-dependent studies on single crystals revealed a hidden antiferromagnetic regime [34].

Another important direction is substitutional carrier tuning, which is expected to maintain the nodal points and near-degeneracies on the nodal plane, but tune the presence of small holelike pockets throughout the BZ, clarifying their role in superconductivity, which is heretofore not considered in detail. These experiments should be pursued in conjunction with revisiting foundational results about this material. In other materials, claims of TRSB superconductivity have become less clear as more experimental evidence emerged, most prominently in Sr<sub>2</sub>RuO<sub>4</sub> [35,36]. With that insight, we emphasize the importance of repeating zero-field  $\mu$ SR measurements as well as other experiments sensitive to TRSB in the superconducting state, on single crystals of LaNiGa<sub>2</sub> where the surface/volume ratio is smaller and the constituency of impurities and inclusions may also be different.

Unconventional superconductors are a very broad class likely to contain a diverse set of pairing mechanisms. The subset of those that break time-reversal symmetry is quite small, and the subset of these TRSB superconductors that do not contain nearby magnetism is smaller yet. The present high-quality data, including the unconventional thin-edge cleave geometry, demonstrate that LaNiGa<sub>2</sub> can continue to yield experimental insights into momentum space electronic structure and can serve as a benchmark for this set of rare superconductors. One other example of TRSB superconductivity without nearby magnetism is 4Hb-TaS<sub>2</sub>. However, being a 2D van der Waals material, 4Hb-TaS<sub>2</sub> likely does not allow for a thin-edge cleave to be achieved in the same way that LaNiGa<sub>2</sub> is shown to here.

## V. CONCLUSIONS

We have performed a comprehensive ARPES study of the purported TRSB superconductor LaNiGa<sub>2</sub> throughout the 3D BZ and demonstrated that this material yields high-quality ARPES spectra. In this paper, we have enhanced our understanding beyond a previous ARPES study on LaNiGa<sub>2</sub> (Ref. [10]) in the following ways: (1) distinct evidence for the nodal plane seen comprehensively throughout the BZ, including cuts both perpendicular and parallel to the nodal plane; (2) showing a filled Ni 3*d* band in XPS measurements and calculations, giving evidence for a nominally nonmagnetic bulk; (3) more accurate assessment of inner potential and correspondence between photon energy and perpendicular momentum, crucial for efficient follow-up ARPES

studies targeting specific band features; and (4) demonstration of thin-edge cleaving in plateletlike specimens to yield ARPES spectra of comparable quality to conventional cleaving, with implications for further surface spectroscopy studies of platelet-shaped specimens. Superconductivity is a low-energy phenomenon which is necessarily affected by the fermiology of a material. This is particularly true in the case of LaNiGa<sub>2</sub> which has an expected gap size of  $k_B T_c \approx 0.6$  meV [14]. The *Cmcm* space group enforces band degeneracies at the  $k_z$  boundary, which constrains any FS that crosses that plane to be degenerate with another. LaNiGa<sub>2</sub> has four FSs which cross the *Z-T* plane, two of which cross the additionally protected *Z-T* line and are degenerate even with SOC. These degenerate FSs are predicted to provide the platform which allows for the interband superconductivity.

Our results have given evidence that predicted degenerate Fermi crossings are present within our measurement resolution and shown that, in other regions of the BZ, there are symmetry-enforced as well as accidental nearly degenerate crossings. These nearly degenerate crossings are most prominent at the  $k_x$  boundaries. Known superconductors in nonsymmorphic space groups are a fruitful avenue to search for TRSB [10], and LaNiGa<sub>2</sub> is emblematic of the important interplay between normal-state fermiology and superconductivity inherent in this approach.

The ARPES data used in this paper are available online [37].

## ACKNOWLEDGMENTS

We thank Filip Ronning, Donghui Lu, Makoto Hashimoto, and Peter Abbamonte for helpful discussions. The synthesis and characterizations were supported by the UC Laboratory Fees Research Program (No. LFR-20-653926). The natural-cleave measurements in this manuscript was supported by AFOSR Grant No. FA9550-18-1-0156, while the thin-edge cleave measurements were supported by the Alfred P. Sloan Foundation (No. FG-2019-12170). Use of the Stanford Synchrotron Radiation Lightsources, SLAC National Accelerator Laboratory, is supported by the U.S. Department of Energy, Office of Science, Office of Basic Energy Sciences under Contract No. DE-AC02-76SF00515. H.J.B. was supported by the NSF-REU Program No. PHY2150515. A.S.B. was supported by the Alfred P. Sloan Foundation (No. FG-2022-19086). This research used resources of the Advanced Light Source, which is a DOE Office of Science User Facility under contract no. DE-AC02-05CH11231. M.S. and S.S. were supported in part by an ALS Doctoral Fellowship in Residence. M.S. and S.S. also acknowledge support by the Dean's faculty fellowship at UC Davis.

[1] A. A. Kordyuk, Iron-based superconductors: Magnetism, superconductivity, and electronic structure (review article), *Low Temp. Phys.* **38**, 888 (2012).

[2] V. B. Zabolotnyy, D. S. Inosov, D. V. Evtushinsky, A. Koitzsch, A. A. Kordyuk, G. L. Sun, J. T. Park, D. Haug, V. Hinkov, A. V. Boris *et al.*, ( $\pi$ ,  $\pi$ ) electronic order in iron arsenide superconductors, *Nature (London)* **457**, 569 (2009).

- [3] E. Fradkin and S. A. Kivelson, Ineluctable complexity, *Nat. Phys.* **8**, 864 (2012).
- [4] M. Hashimoto, I. M. Vishik, R.-H. He, T. P. Devereaux, and Z.-X. Shen, Energy gaps in high-transition-temperature cuprate superconductors, *Nat. Phys.* **10**, 483 (2014).
- [5] T. Yokoya, A. Chainani, T. Takahashi, H. Katayama-Yoshida, M. Kasai, and Y. Tokura, Extended van hove singularity in a noncuprate layered superconductor  $\text{Sr}_2\text{RuO}_4$ , *Phys. Rev. Lett.* **76**, 3009 (1996).
- [6] Q. H. Wang, C. Platt, Y. Yang, C. Honerkamp, F. C. Zhang, W. Hanke, T. M. Rice, and R. Thomale, Theory of superconductivity in a three-orbital model of  $\text{Sr}_2\text{RuO}_4$ , *Europhys. Lett.* **104**, 17013 (2013).
- [7] V. Sunko, E. Abarca Morales, I. Marković, M. E. Barber, D. Milosavljević, F. Mazzola, D. A. Sokolov, N. Kikugawa, C. Cacho, P. Dudin *et al.*, Direct observation of a uniaxial stress-driven lifshitz transition in  $\text{Sr}_2\text{RuO}_4$ , *npj Quantum Mater.* **4**, 46 (2019).
- [8] T. Shang, M. Smidman, S. K. Ghosh, C. Baines, L. J. Chang, D. J. Gawryluk, J. A. T. Barker, R. P. Singh, D. M. Paul, G. Balakrishnan *et al.*, Time-reversal symmetry breaking in Re-based superconductors, *Phys. Rev. Lett.* **121**, 257002 (2018).
- [9] S. K. Ghosh, M. Smidman, T. Shang, J. F. Annett, A. D. Hillier, J. Quintanilla, and H. Yuan, Recent progress on superconductors with time-reversal symmetry breaking, *J. Phys.: Condens. Matter* **33**, 033001 (2021).
- [10] J. R. Badger, Y. Quan, M. C. Staab, S. Sumita, A. Rossi, K. P. Devlin, K. Neubauer, D. S. Shulman, J. C. Fetting, P. Klavins *et al.*, Dirac lines and loop at the Fermi level in the time-reversal symmetry breaking superconductor  $\text{LaNiGa}_2$ , *Commun. Phys.* **5**, 22 (2022).
- [11] A. T. Rømer, A. Kreisel, M. A. Müller, P. J. Hirschfeld, I. M. Eremin, and B. M. Andersen, Theory of strain-induced magnetic order and splitting of  $T_c$  and  $T_{\text{TRSB}}$  in  $\text{Sr}_2\text{RuO}_4$ , *Phys. Rev. B* **102**, 054506 (2020).
- [12] D. Aoki, J.-P. Brison, J. Flouquet, K. Ishida, G. Knebel, Y. Tokunaga, and Y. Yanase, Unconventional superconductivity in  $\text{UTe}_2$ , *J. Phys.: Condens. Matter* **34**, 243002 (2022).
- [13] C. Farhang, N. Zaki, J. Wang, G. Gu, P. D. Johnson, and J. Xia, Revealing the origin of time-reversal symmetry breaking in Fe-chalcogenide superconductor  $\text{FeTe}_{1-x}\text{Se}_x$ , *Phys. Rev. Lett.* **130**, 046702 (2023).
- [14] Y. Quan, V. Taufour, and W. E. Pickett, Nonsymmorphic band sticking in a topological superconductor, *Phys. Rev. B* **105**, 064517 (2022).
- [15] D. J. Singh, Electronic structure and fermiology of superconducting  $\text{LaNiGa}_2$ , *Phys. Rev. B* **86**, 174507 (2012).
- [16] N. L. Zeng and W. H. Lee, Superconductivity in the Ni-based ternary compound  $\text{LaNiGa}_2$ , *Phys. Rev. B* **66**, 092503 (2002).
- [17] A. D. Hillier, J. Quintanilla, B. Mazidian, J. F. Annett, and R. Cywinski, Nonunitary triplet pairing in the centrosymmetric superconductor  $\text{LaNiGa}_2$ , *Phys. Rev. Lett.* **109**, 097001 (2012).
- [18] H. G. Suh, Y. Yu, T. Shishidou, M. Weinert, P. M. R. Brydon, and D. F. Agterberg, Superconductivity of anomalous pseudospin in nonsymmorphic materials, *Phys. Rev. Res.* **5**, 033204 (2023).
- [19] Z. Hao, W. Chen, Y. Wang, J. Li, X. M. Ma, Y. J. Hao, R. Lu, Z. Shen, Z. Jiang, W. Liu *et al.*, Multiple dirac nodal lines in an in-plane anisotropic semimetal, *Phys. Rev. B* **104**, 115158 (2021).
- [20] S. Xiao, W.-H. Jiao, Y. Lin, Q. Jiang, X. Yang, Y. He, Z. Jiang, Y. Yang, Z. Liu, M. Ye *et al.*, Dirac nodal lines in the quasi-one-dimensional ternary Telluride  $\text{TaPtTe}_5$ , *Phys. Rev. B* **105**, 195145 (2022).
- [21] See Supplemental Material at <http://link.aps.org/supplemental/10.1103/PhysRevB.110.165115> for additional ARPES data and DFT calculations with orbital projections.
- [22] P. Blaha, K. Schwarz, F. Tran, R. Laskowski, G. K. H. Madsen, and L. D. Marks, WIEN2K: An APW+lo program for calculating the properties of solids, *J. Chem. Phys.* **152**, 074101 (2020).
- [23] J. P. Perdew, K. Burke, and M. Ernzerhof, Generalized gradient approximation made simple, *Phys. Rev. Lett.* **77**, 3865 (1996).
- [24] A. Damascelli, Probing the electronic structure of complex systems by ARPES, *Phys. Scr.* **2004**, 61 (2004).
- [25] P. Sherpa, I. Vinograd, Y. Shi, S. A. Sreedhar, C. Chaffey, T. Kissikov, M.-C. Jung, A. S. Botana, A. P. Dioguardi, R. Yamamoto *et al.*, Absence of strong magnetic fluctuations or interactions in the normal state of  $\text{LaNiGa}_2$ , *Phys. Rev. B* **109**, 125113 (2024).
- [26] S. Moser, An experimentalist's guide to the matrix element in angle resolved photoemission, *J. Electron Spectrosc. Relat. Phenom.* **214**, 29 (2017).
- [27] S. Tanuma, C. Powell, and D. Penn, Proposed formula for electron inelastic mean free paths based on calculations for 31 materials, *Surf. Sci.* **192**, L849 (1987).
- [28] V. Strocov, Intrinsic accuracy in 3-dimensional photoemission band mapping, *J. Electron Spectrosc. Relat. Phenom.* **130**, 65 (2003).
- [29] Z. F. Weng, J. L. Zhang, M. Smidman, T. Shang, J. Quintanilla, J. F. Annett, M. Nicklas, G. M. Pang, L. Jiao, W. B. Jiang *et al.*, Two-gap superconductivity in  $\text{LaNiGa}_2$  with nonunitary triplet pairing and even parity gap symmetry, *Phys. Rev. Lett.* **117**, 027001 (2016).
- [30] S. Sundar, M. Yakovlev, N. Azari, M. Abedi, D. M. Broun, H. U. Özdemir, S. R. Dunsiger, D. Zackaria, H. Bowman, P. Klavins *et al.*, Gap structure of the nonsymmorphic superconductor  $\text{LaNiGa}_2$  probed by  $\mu\text{SR}$ , *Phys. Rev. B* **109**, 104517 (2024).
- [31] S. K. Ghosh, G. Csire, P. Whittlesea, J. F. Annett, M. Gradhand, B. Újfalussy, and J. Quintanilla, Quantitative theory of triplet pairing in the unconventional superconductor  $\text{LaNiGa}_2$ , *Phys. Rev. B* **101**, 100506(R) (2020).
- [32] S. Ghimire, K. R. Joshi, E. H. Krenkel, M. A. Tanatar, Y. Shi, M. Kończykowski, R. Grasset, V. Taufour, P. P. Orth, M. S. Scheurer *et al.*, Electron irradiation reveals robust fully gapped superconductivity in  $\text{LaNiGa}_2$ , *Phys. Rev. B* **109**, 024515 (2024).
- [33] H. M. Tütüncü and G. P. Srivastava, Origin of superconductivity in layered centrosymmetric  $\text{LaNiGa}_2$ , *Appl. Phys. Lett.* **104**, 022603 (2014).
- [34] J. F. Landaeta, D. Subero, P. Machado, F. Honda, and I. Bonalde, Unconventional superconductivity and an ambient-pressure magnetic quantum critical point in single-crystal  $\text{LaNiC}_2$ , *Phys. Rev. B* **96**, 174515 (2017).
- [35] A. Pustogov, Y. Luo, A. Chronister, Y. S. Su, D. A. Sokolov, F. Jerzembeck, A. P. Mackenzie, C. W. Hicks, N. Kikugawa, S. Raghu *et al.*, Constraints on the superconducting order parameter in  $\text{Sr}_2\text{RuO}_4$  from oxygen-17 nuclear magnetic resonance, *Nature (London)* **574**, 72 (2019).



- [36] A. Chronister, A. Pustogow, N. Kikugawa, D. A. Sokolov, F. Jerzembeck, C. W. Hicks, A. P. Mackenzie, E. D. Bauer, and S. E. Brown, Evidence for even parity unconventional superconductivity in  $\text{Sr}_2\text{RuO}_4$ , *Proc. Natl. Acad. Sci. USA* **118**, e2025313118 (2021).
- [37] M. Staab, and I. Vishik, “Symmetry Enforced Fermi Surface Degeneracies Observed in Time-Reversal Symmetry-Breaking Superconductor  $\text{LaNiGa}_2$  [Data set]”, Zenodo, doi:10.5281/zenodo.12786386.